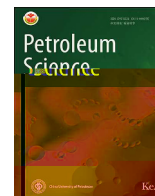




Contents lists available at ScienceDirect

Petroleum Science

journal homepage: www.keaipublishing.com/en/journals/petroleum-science



Original Paper

A quantitative interpretation method of gas kick driven by physics-informed neural network

Hong-Wei Yang^a, Biao Wang^{a,*}, Jun Li^{a,b,d}, Geng Zhang^a, Gong-Hui Liu^{a,c,d}, Jia-Hao Zhan^a, Zhen-Yu Long^a, Chao Wang^e

^a School of Petroleum Engineering, China University of Petroleum (Beijing), Beijing 102249, China
^b School of Mechanical Engineering, China University of Petroleum (Beijing), Beijing 102249, China
^c School of Information Science and Technology, China University of Petroleum (Beijing), Beijing 102249, China
^d School of Geology, China University of Petroleum (Beijing), Beijing 102249, China
^e School of Chemical Engineering, China University of Petroleum (Beijing), Beijing 102249, China

ARTICLE INFO

Received 20 July 2025
 Received in revised form 20 January 2026
 Accepted 20 January 2026
 Available online 25 January 2026

Edited by Jia-Jia Fei

Gas kick
 Quantitative interpretation
 Physics-informed neural network
 Downhole dual measurement tools
 Partial differential equation

ABSTRACT

To address the challenges associated with predicting wellbore fluid flow behavior and gas kick rates in deep, complex formations following gas kick events, this study develops a quantitative interpretation method of gas kick driven by physics-informed neural network (PINN). The proposed method integrates a physical model of gas–liquid two-phase flow in the wellbore into the neural network by formulating it as a loss function, leveraging annulus temperature and pressure data obtained from downhole dual measurement tools. The feasibility and effectiveness of this method are evaluated through comparative analysis. The result indicates that during gas kick occurrences, this method achieves mean relative errors of 8.49% and 9.07% for the predicted gas volume fraction and apparent

conditions. Integrating this method with downhole dual measurement tools can provide valuable guidance for blowout risk assessment, well-control method selection, and well-killing parameter design after a gas kick.

© 2026 The Authors. Publishing services by Elsevier B.V. on behalf of KeAi Communications Co. Ltd. This is an open access article under the CC BY-NC-ND license (<http://creativecommons.org/licenses/by-nc-nd/4.0/>).

1. Introduction

Gas kick refers to the phenomenon in which formation gas invades the wellbore due to the differential pressure when formation pressure exceeds wellbore pressure (Mitchell and Miska, 2011). As oil and gas exploration advances toward deep, complex formations, drilling operations increasingly encounter challenging geological and environmental conditions, including complex formation pressure systems, developed fracture-cavity systems, and narrow safe density windows, resulting in frequent occurrences of

gas kicks. Failure to detect gas kicks promptly or control them effectively can readily lead to serious drilling incidents, such as blowouts (Karimi Vajargah et al., 2013; Bhandari et al., 2015; Li et al., 2022b). Therefore, effectively mitigating the risk of gas kicks has become a critical issue requiring urgent attention (Galdino et al., 2019; Atchison, 2022; Wu et al., 2022).

Currently, in response to significant challenges to safe and efficient drilling posed by gas kicks, extensive research has focused primarily on early detection and quantitative interpretation of gas kicks. Early detection techniques facilitate timely well control measures to balance formation pressure and reduce gas content in the wellbore. These techniques include inlet-outlet flow rate difference methods (Ali et al., 2013), mud pit level monitoring methods (Blue et al., 2019; Lafond et al., 2019), acoustic detection methods (Dashti and Riazi, 2014; Johnson et al., 2014; Toskey,

* Corresponding author.
 E-mail address: wangbiao_cup@163.com (B. Wang).
 Peer review under the responsibility of China University of Petroleum (Beijing).

2015; Wang et al., 2018), pressure wave detection methods (Stokka et al., 1993; Li et al., 2022a), and downhole measurement-while-drilling (MWD) detection methods (Nayeem et al., 2016; Samuel, 2018; Sule et al., 2019; Yang et al., 2019; Wang et al., 2020b). Among these, the downhole MWD detection method demonstrates high accuracy and timeliness, particularly following the development of downhole dual measurement tools (Wang et al., 2020a), effectively overcoming the high false-alarm rate issue associated with relying solely on parameters measured at a single downhole point.

This study focuses on the quantitative interpretation of gas kicks, specifically how to accurately determine the gas-liquid two-phase fluid distribution in the wellbore and the rate of gas invasion following a gas kick. Accurate interpretation is critical for guiding risk assessment, selection of well-killing methods, and design of well-killing parameters (Liu et al., 2021). Traditionally, gas kick rates are estimated based on the incremental volume increase in the mud pit and the duration of the gas kick, providing a simple yet low-accuracy approach. Some researchers have proposed quantitative interpretation methods based on fluid properties. For instance, Wang et al. (2022) experimentally analyzed the relationship between gas fraction and the velocity and attenuation characteristics of low-frequency elastic waves, establishing a mapping relationship between elastic wave responses and gas fraction. Some researchers (Zhou et al., 2017; Yin et al., 2020; Gu et al., 2021; Indimath et al., 2023) developed quantitative characterization models of gas fraction based on features such as mean amplitude and frequency domain signals of Doppler ultrasound. Wang et al. (2017) established a relationship between gas fraction and dimensionless logging-while-drilling resistivity, achieving an average relative error of 5% in experimental data. However, these methods are susceptible to interference from bubble and cuttings distribution, drill string vibration, and high temperature and pressure conditions. With advances in multiphase flow theory, numerical models now describe multiphase fluid flow in the wellbore post-gas kick, framing predictions of gas fraction and gas kick rate as inverse problems of the multiphase flow model. Obi et al. (2022a, 2022b) conducted experimental gas kick simulations combined with numerical models, deriving nonlinear expressions relating gas kick rate to gas fraction, riser pressure, and casing pressure. Several researchers (Gravdal et al., 2010; Zhou and Nygaard, 2011; Hauge et al., 2012; Nikoofard et al., 2015; Jiang et al., 2019) integrated multiphase flow models with unscented Kalman filter (UKF) and nonlinear observers, utilizing multi-source measurements such as bottom-hole pressure, riser pressure, and outlet flow rate for predictions. Another group of researchers (Song et al., 2011; Xia et al., 2019; Wang et al., 2023a; Yin et al., 2024) used particle swarm optimization (PSO) and genetic algorithms (GA) to minimize errors between multi-source measurements and computed values, determining gas kick rate, fluid distribution in the wellbore, and formation parameters. These methods rely heavily on numerical model reliability and have high requirements for numerical solution stability and truncation error accuracy.

In recent years, machine learning has been widely used for the intelligent detection of drilling anomalies because of its strong nonlinear fitting capability. Researchers have developed early gas kick detection models based on machine learning methods such as random forest (Shi et al., 2020), K-nearest neighbor (Alouhali et al., 2018), Bayesian networks (Bhandari et al., 2015; Nhat et al., 2020), long short-term memory networks (Yin et al., 2021; Zhu et al., 2023), and ensemble learning methods (Wang et al., 2023b). Yin et al. (2022) established a real-time intelligent prediction model for bottom-hole gas kick rates by combining ground logging and downhole multi-source measurement-while-drilling data using

an LSTM network. Although these intelligent models can automatically capture complex mappings between feature parameters and gas kick and achieve good results on tested datasets, their robustness remains limited due to scarce data samples and significant variability among different drilling blocks. Additionally, purely data-driven intelligent models suffer from ambiguous intermediate computational processes and poor interpretability. Physics-informed neural network (PINN), an emerging branch in the field of deep learning (Dissanayake et al., 2001; Zhao et al., 2024), incorporate physical knowledge into neural networks and can learn highly generalized models from limited or even unlabeled data. Currently, PINN has been successfully applied to a wide range of problems, including solving fundamental equations (Pang et al., 2019; Zhang et al., 2019, 2020; Lu et al., 2021), simulating flow in porous media (Raissi et al., 2020; Wang et al., 2020; Yan et al., 2022), and parameter inversion (Amini et al., 2023; Kapoor et al., 2023). In the coupling research of the PINN method with drilling engineering, Xu et al. (2023) combined a wellbore gas-liquid two-phase flow model with neural networks to construct an adaptive PINN model for annulus pressure prediction in two-phase flow. Liu et al. (2025) developed a PINN-driven approach for solving wellbore temperature fields, which significantly improved computational speed while ensuring accuracy. Some researchers (Jeong et al., 2020; Jan et al., 2022; Gkionis et al., 2025) integrated physical knowledge with neural networks to establish a PINN-based intelligent diagnosis approach for drill string washout, markedly enhancing the recognition accuracy of complex downhole conditions. However, most of these studies have focused on modeling and simulating wellbore pressure and temperature fields, with some addressing qualitative identification of complex downhole conditions. Research on quantitative interpretation methods for complex conditions such as gas kick remains relatively limited.

Compared to traditional numerical methods such as finite difference and finite volume methods, PINN significantly improves computational accuracy through parallel computations and global optimization strategies without requiring mesh discretization or explicitly defined initial conditions. This advantage is particularly important for accurate predictions of multiphase fluid flow conditions and gas kick rates in the wellbore following gas kick events. This study develops a quantitative interpretation method of gas kick driven by physics-informed neural networks by integrating a physical model of gas-liquid two-phase flow in the wellbore and neural networks, utilizing annulus temperature and pressure data measured by downhole dual measurement tools. The proposed method enables intelligent prediction of the gas volume fraction and apparent gas phase velocity between the dual measurement points, as well as the bottomhole gas kick rate. The feasibility and advantages of this approach were evaluated through analysis conducted on a simulated well and comparisons with the UKF and GA.

2. Physical model of gas-liquid two-phase flow in the wellbore

The physical model of gas-liquid two-phase flow in the wellbore primarily consists of mass conservation and momentum conservation equations, describing the flow behavior of gas-liquid mixtures in the wellbore following a gas kick. To effectively simplify calculations, the following assumptions are made according to actual fluid flow behavior within the wellbore: (1) Drilling fluid flows one-dimensionally in the wellbore, with uniform parameters such as temperature, pressure, density, and velocity in the radial direction (Sun et al., 2017); (2) Mass transfer between gas and liquid phases is neglected; (3) The temperature distribution in the wellbore follows a uniform thermal gradient;

(4) The effects of temperature and pressure on drilling fluid properties are considered; (5) The slip effect between gas and liquid phases is accounted for.

21

(1) Mass conservation equation

According to the principle of mass conservation (Udegbumam et al., 2014), the rate of change in fluid mass within a differential control volume over a period of time is equal to the difference between the mass of fluid exiting and entering the volume. Accordingly, the mass conservation equations for the gas and liquid phases can be expressed as:

$$-\frac{\partial(\rho_g v_g)}{\partial t} + \frac{\partial(\rho_g v_g)}{\partial y} = -q_g \quad (1)$$

$$-\frac{\partial(\rho_l v_l)}{\partial t} + \frac{\partial(\rho_l v_l)}{\partial y} = 0 \quad (2)$$

where, t is time, s; y is spatial coordinate, m; ρ_g and ρ_l are the densities of the gas and liquid phases, respectively, kg/m^3 ; A is the cross-sectional area of the wellbore annulus, m^2 ; v_g and v_l are the volume fractions of the gas and liquid phases, respectively, satisfying the relation $v_g + v_l = 1$; v_g and v_l are the actual velocities of the gas and liquid phases, respectively, m/s; q_g is the gas kick rate per unit thickness of the reservoir, $\text{kg}/\text{s}\cdot\text{m}$.

(2) Momentum conservation equation

According to the principle of momentum conservation (Udegbumam et al., 2014), the rate of change of fluid momentum within an elemental control volume over time equals the sum of external forces acting on it. Based on

where, the calculation methods of ρ_1 , ρ_2 , and ρ_3 are as follows:

$$\left\{ \begin{array}{l} \rho_1 = \frac{33.486 \cdot 10^{-7} \rho_g}{0.5 \mu_g w} \\ \rho_2 = \lg(\text{---}) \end{array} \right.$$

$$\frac{(\rho_g g)_1 \ddagger (\rho_g g)_1^1 (\rho_g g)_1^1 (\rho_g g)_1^1}{2} \ddagger \frac{(\rho_g g v_g)_1 (\rho_g g v_g)_1^1}{y} \sim (g) \quad (17)$$

$$\frac{-\rho_{11} \uparrow \ddagger -\rho_{11} \uparrow \ddagger -\rho_{11} \uparrow \ddagger -\rho_{11} \uparrow \ddagger}{2} \ddagger \frac{-\rho_{11} v_{11} \uparrow \ddagger -\rho_{11} v_{11} \uparrow \ddagger}{y} \sim 0 \quad (18)$$

The discretized form of the momentum conservation equation is given by:

$$\frac{-\rho_{11} \uparrow \ddagger -\rho_{11} \uparrow \ddagger -\rho_{11} \uparrow \ddagger -\rho_{11} \uparrow \ddagger}{2}$$

$$\frac{\partial \bar{y}}{\partial \bar{t}} = \frac{\bar{\rho}_1 \bar{v}_1}{\bar{y}} \quad (32)$$

$$\frac{\partial \bar{y}}{\partial \bar{t}} = \frac{(\bar{\rho}_g \bar{v}_g + \bar{\rho}_1 \bar{v}_1)}{\bar{y}} + \frac{(\bar{\rho}_g \bar{v}_g^2 + \bar{\rho}_1 \bar{v}_1^2)}{\bar{y}} + \frac{\bar{y}}{4} + \frac{\bar{y}^*}{2} (\bar{\rho}_g + \bar{\rho}_1) \bar{\rho} \cos \theta \quad (33)$$

where, \bar{y} , \bar{t} , \bar{v}_g , \bar{v}_1 , $\bar{\rho}_g$, $\bar{\rho}_1$, $\bar{\rho}$, \bar{y}^* , \bar{t}^* , \bar{v}^* , $\bar{\rho}^*$, $\bar{\rho}_f^*$ represent the dimensionless spatial coordinate, dimensionless time, dimensionless actual gas phase velocity, dimensionless actual drilling fluid velocity, dimensionless gas density, liquid density, dimensionless annulus pressure, and dimensionless frictional pressure loss, respectively. \bar{y}^* , \bar{t}^* , \bar{v}^* , $\bar{\rho}^*$, $\bar{\rho}_f^*$ represent the reference values for spatial coordinate, time, fluid velocity, fluid density, annulus pressure, and frictional pressure loss, respectively. \bar{y}_4 and \bar{y}_5 are

Expert knowledge constraints can further enhance the physical plausibility of neural network predictions. For example, the outputs of the neural network (annulus pressure, volume fraction, and actual fluid velocity) must not be less than zero. In addition, for deep oil and gas wells experiencing gas kicks, the gas volume fraction between the dual measurement points generally does not exceed 0.2. Furthermore, at an

where, $v_1(\bar{t}, \bar{y}; \theta_1)$ is the dimensionless actual liquid phase velocity predicted by Network A; $p_2(\bar{t}, \bar{y}; \theta_2)$ is the dimensionless annulus pressure predicted by Network B; $v_3(\bar{t}, \bar{y}; \theta_3)$ is the dimensionless actual gas phase velocity predicted by Network C; $\phi_4(\bar{t}, \bar{y}; \theta_4)$ is the gas volume fraction predicted by Network D; N is the number of spatiotemporal points.

The expression for L_{BC} is:

$$L_{BC} = \frac{1}{N} \sum_{i=1}^N \left[\tilde{p}_2(\bar{t}_i, \bar{y}_i; \theta_2) - v_1(\bar{t}_i, \bar{y}_i) \right]^2 + \frac{1}{N} \sum_{i=1}^N \left[\tilde{p}_2(\bar{t}_i, \bar{y}_i; \theta_2) - p_2(\bar{t}_i, \bar{y}_i) \right]^2 + \frac{1}{N} \sum_{i=1}^N \left[\tilde{v}_1(\bar{t}_i, \bar{y}_i; \theta_1) - v_3(\bar{t}_i, \bar{y}_i; \theta_3) - \frac{v_1(\bar{t}_i, \bar{y}_i)}{\rho_g(\bar{t}_i, \bar{y}_i)} \right]^2 \quad (42)$$

where, $\tilde{p}_2(\bar{t}_i, \bar{y}_i; \theta_2)$ is the predicted pressure at the far-bit position, MPa; $\tilde{p}_2(\bar{t}_i, \bar{y}_i; \theta_2)$ is the predicted pressure at the near-bit position, MPa; $\tilde{v}_1(\bar{t}_i, \bar{y}_i; \theta_1)$ is the predicted actual liquid phase velocity at the near-bit position, m/s; N is the number of time points.

The expression for L_{EK} is:

$$L_{EK} = \frac{1}{N} \sum_{i=1}^N \left[\begin{aligned} &\max(0, \tilde{p}_2(\bar{t}_i, \bar{y}_i; \theta_2) - p_2(\bar{t}_i, \bar{y}_i)) + \max(0, v_3(\bar{t}_i, \bar{y}_i; \theta_3) - v_1(\bar{t}_i, \bar{y}_i; \theta_1)) \\ &+ \max(0, \tilde{p}_2(\bar{t}_i, \bar{y}_i; \theta_2) - p_2(\bar{t}_i, \bar{y}_i)) + \max(0, v_3(\bar{t}_i, \bar{y}_i; \theta_3) - v_1(\bar{t}_i, \bar{y}_i; \theta_1)) \\ &+ \max(0, \phi_4(\bar{t}_i, \bar{y}_i; \theta_4) - 0.2) \end{aligned} \right] + \frac{1}{N} \sum_{i=1}^N \left[\max(0, -(\tilde{v}_1(\bar{t}_i, \bar{y}_i; \theta_1) - v_3(\bar{t}_i, \bar{y}_i; \theta_3))) + \max(0, -(\tilde{v}_1(\bar{t}_i, \bar{y}_i; \theta_1) - v_3(\bar{t}_i, \bar{y}_i; \theta_3))) \right] + \frac{1}{N} \sum_{i=1}^N \left[\tilde{p}_2(\bar{t}_i, \bar{y}_i) - p_2(\bar{t}_i, \bar{y}_i) - \sum_{i=1}^N (\rho_g(\bar{t}_i, \bar{y}_i) v_3(\bar{t}_i, \bar{y}_i; \theta_3) + \rho_1(\bar{t}_i, \bar{y}_i) (1 - \phi_4(\bar{t}_i, \bar{y}_i; \theta_4))) y + \left(\frac{f}{y}(\bar{t}_i, \bar{y}_i) \right) y \right]^2 + \frac{1}{N} \left[\phi_4(\bar{t}_i, \bar{y}_i; \theta_4) - \frac{v_3(\bar{t}_i, \bar{y}_i; \theta_3) v_1(\bar{t}_i, \bar{y}_i; \theta_1)}{v_g^* (\phi_4(\bar{t}_i, \bar{y}_i; \theta_4) + v_1(\bar{t}_i, \bar{y}_i; \theta_1) (1 - \phi_4(\bar{t}_i, \bar{y}_i; \theta_4)))} + v_{gr}(\bar{t}_i, \bar{y}_i) \right]^2 \quad (43)$$

where, N is the total number of spatiotemporal points within the solution domain and on its boundaries.

Based on the predicted actual gas velocity and the measured pressure and temperature at the bottomhole, the gas kick rate under standard conditions can be derived using the gas mass conservation law as follows:

$$\hat{Q}_{g_{std}} = \frac{\tilde{v}_3(\bar{t}_i, \bar{y}_i; \theta_3) \tilde{v}_4(\bar{t}_i, \bar{y}_i; \theta_4) \frac{p_{std}}{Z T_{std}}}{\rho_g} \quad (44)$$

where, $\hat{Q}_{g_{std}}$ is the predicted gas kick rate at the bottomhole under standard conditions, m³/s; $\tilde{v}_3(\bar{t}_i, \bar{y}_i; \theta_3)$ is the predicted actual gas phase velocity at the near-bit position, m/s; $\tilde{v}_4(\bar{t}_i, \bar{y}_i; \theta_4)$ is the predicted gas volume fraction at the near-bit position; T_{std} is the measured temperature at the near-bit position, °C.

It should be noted that the thermophysical properties of drilling fluid and gas, including density and viscosity, are functions of temperature and pressure at each spatiotemporal location within the solution domain. To reduce training cost and enhance the convergence of the PINN, this study adopts an isothermal gradient-based approach to estimate the temperature distribution throughout the domain. The justification for this method is presented in [Appendix C](#).

3.3 Training

During the training of PINN, if the gradient vector of a specific loss term with respect to the network parameters is significantly larger than those of other terms, it may dominate the overall gradient used to update the network. This phenomenon can cause the PINN outputs to rely heavily on the accurate enforcement of boundary conditions, potentially limiting model performance. To address this issue, this study adopts the GradNorm algorithm proposed by [Chen et al. \(2018\)](#), which adaptively balances the contributions of each loss term by adjusting their weights based

on gradient magnitudes. The method can be formulated as follows:

$$w_i = \frac{1}{\sum_{j=1}^M w_j} \frac{GN_i}{GN_j} \quad (45)$$

where, the expression for GN_i is:

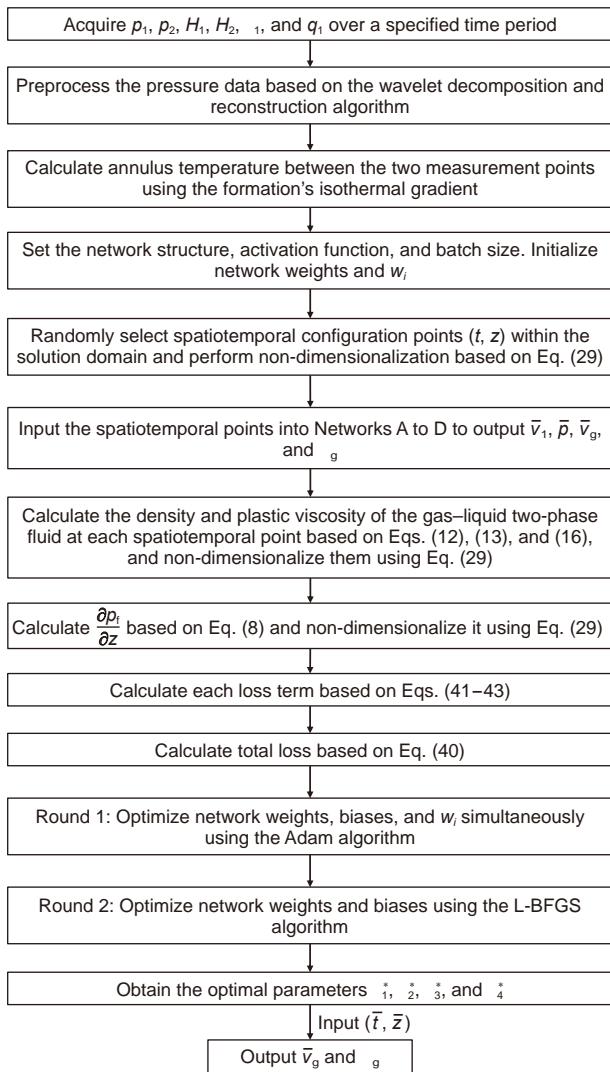


Fig. 4. Flowchart of the PINN-based quantitative interpretation process for gas kick.

$$GN = \sum_{i=1}^3 \left| \left(\sum_{j=1}^3 \theta_j \right) \right|, \quad \theta_j = \frac{\gamma \cdot \dots \theta_1, \theta_2, \theta_3, \theta_4^\dagger}{\theta_j}, \quad s = \frac{\sum_{i=1}^3 \dots}{\dots 0^\dagger} \tag{46}$$

The adaptive training weights allow the network to automatically adjust for the imbalance among the gradients of different loss terms. Meanwhile, the weights and biases of Networks A, B, C, and D are optimized by minimizing the total loss function during training:

$$\theta_1 = \theta_1^\dagger \gamma \frac{\dots \theta_1, \theta_2, \theta_3, \theta_4^\dagger}{\theta_1} \tag{47}$$

$$\theta_2 = \theta_2^\dagger \gamma \frac{\dots \theta_1, \theta_2, \theta_3, \theta_4^\dagger}{\theta_2} \tag{48}$$

$$\theta_3 = \theta_3^\dagger \gamma \frac{\dots \theta_1, \theta_2, \theta_3, \theta_4^\dagger}{\theta_3} \tag{49}$$

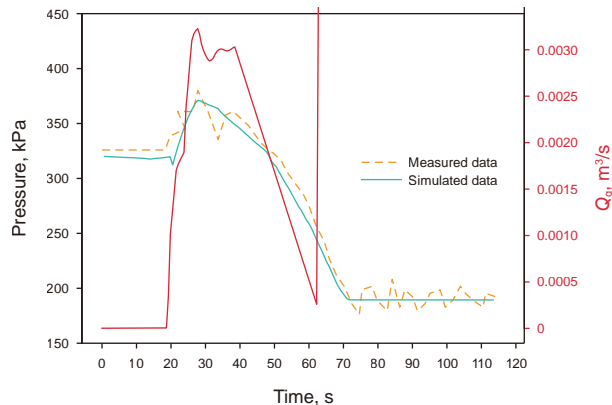


Fig. 5. Comparison of measured and simulated pressure results.

$$\theta_4 = \theta_4^\dagger \gamma \frac{\dots \theta_1, \theta_2, \theta_3, \theta_4^\dagger}{\theta_4} \tag{50}$$

where, γ and θ_j are the learning rate; θ_j^\dagger is the loss item corresponding to θ_j ; $\dots 0^\dagger$ is the loss when the network weight is set to its initial value; \dots is the scaling factor.

The PINN illustrated in Fig. 3 is developed using the PyTorch deep learning framework. A two-stage optimization strategy, integrating global and local optimization, is applied during training. Initially, the Adam optimizer is employed for a predefined number of iterations to update the network weights and biases, while simultaneously adjusting the weights of each loss term. In the subsequent stage, the loss weights are fixed, and the network parameters are further optimized using the second-order L-BFGS algorithm. The workflow for predicting gas volume fraction, apparent gas phase velocity, and gas kick rate with the PINN is presented in Fig. 4.

3

The mean relative error (MRE), root mean square error (RMSE), and mean absolute error (MAE) are used as evaluation metrics for assessing the prediction accuracy of gas volume fraction, apparent

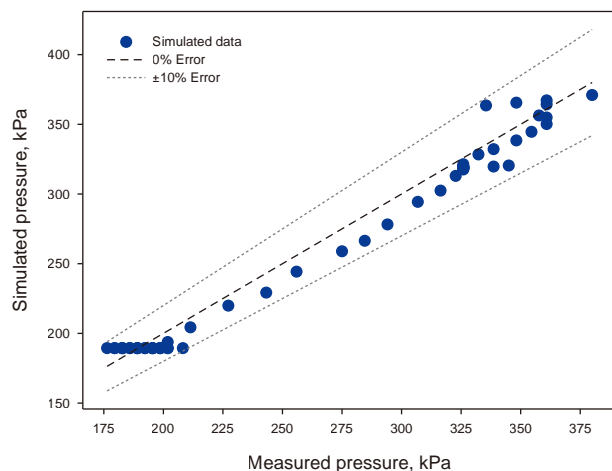


Fig. 6. Analysis of pressure prediction errors.

Table 2
Basic parameters of the simulated well.

| Parameter | Value | Parameter | Value |
|---|-------|--|------------|
| Well depth, m | 5000 | Surface temperature, C | 20 |
| Outer diameter of drill pipe, mm | 127 | Geothermal gradient, C/m | 0.028 |
| Diameter of borehole, mm | 215.9 | Pump discharge rate, m ³ /s | 0.028 |
| Drilling fluid density, kg/m ³ | 1200 | Formation pressure, MPa | 62 |
| Drilling fluid viscosity, mPa s | 10 | Wellhead backpressure, MPa | 1 |
| Reservoir permeability, mD | 1.5 | Skin factor | 2 |
| Reservoir thickness, m | 10 | Reservoir drainage radius, m | 120 |
| Near-bit sub depth, m | 5000 | Drilling fluid system | Water-base |
| Far-bit sub depth, m | 4970 | Well inclination angle, | 0 |

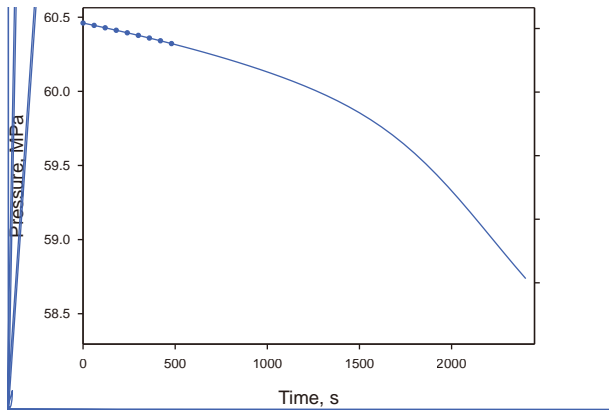


Fig. 7. Response patterns of annulus pressure and gas kick rate at dual measurement points during the gas kick process.

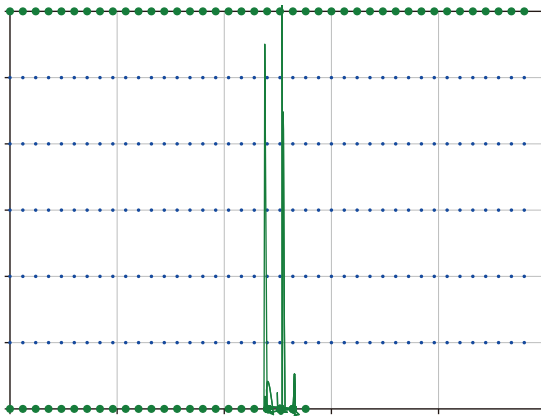


Fig. 8. Distribution of training samples (Green indicates spatiotemporal points at the boundaries; Blue indicates spatiotemporal points within the solution domain).

gas phase velocity, and gas kick rate. For a given true value, smaller values of these metrics indicate lower prediction errors. It should be noted that when the true values are small, the MRE may be disproportionately amplified. In such cases, RMSE and MAE are considered the primary evaluation indicators.

$$\text{MRE} \sim \frac{1}{n} \sum_{j=1}^n \left| \frac{\hat{y}_j - y_j}{y_j} \right| \quad 100\% \quad (51)$$

$$\text{RMSE} \sim \sqrt{\frac{1}{n} \sum_{j=1}^n (\hat{y}_j - y_j)^2} \quad (52)$$

$$\text{MAE} \sim \frac{1}{n} \sum_{j=1}^n |\hat{y}_j - y_j| \quad (53)$$

where, y_j is the true value; \hat{y}_j is the predicted value; n is the number of samples.

4. Results and discussion

1

Since no gas kick events occurred during the use of the downhole dual measurement tools, the pressure data at the far-bit and near-bit positions used to train the PINN were generated by combining the simulated values from the physical model of gas–liquid two-phase flow in the wellbore with added noise. After evaluating the feasibility of the proposed method, it will be integrated with the downhole dual measurement tools. Once a gas kick occurs, the method can then be used to intelligently predict parameters such as gas volume fraction, apparent gas phase velocity, and gas kick rate, thereby assisting field personnel in selecting appropriate well control methods and designing well control parameters. Before generating the synthetic training data, it is necessary to validate the accuracy of the physical model of gas–liquid two-phase flow in the wellbore. In this study, the accuracy and reliability of the physical model were verified using two types of experimental data, namely the laboratory-scale data presented by Yang et al. (2019) and the full-scale experimental well data presented by Lopes (1997), respectively. The verification results based on the full-scale experimental well data are provided in Appendix D. The laboratory experiment simulated the variation of annulus pressure during the gas kick process using a vertical coaxial annular pipe. The pipe had a length of 27 m, with the outer pipe having an inner diameter of 221.0 mm and the inner pipe having an outer diameter of 127.0 mm. Clear water was used as the liquid phase with a flow rate of 0.005 m³/s. Air was used as the gas phase medium. When steady-state gas–liquid two-phase flow was established in the annulus, the gas flow rate was 0.003 m³/s.

Fig. 5 presents the time-dependent curves of simulated and measured pressures at a location 5 m above the bottom of the annular pipe. During the initial gas injection phase, the gas front

had not yet reached the measurement point. As a result, the fluid density above the measurement point remained constant. However, gas injection increased the fluid velocity and the frictional pressure loss, leading to a rise in pressure at the measurement location. Once the gas front arrived at the measurement point, the fluid density above the point began to decrease, causing a

subsequent drop in pressure. When the annulus became fully charged with gas and the gas injection rate at the bottom stabilized, the gas-liquid two-phase flow reached a steady-state condition, and the ~~pressure~~ **prestant.at**

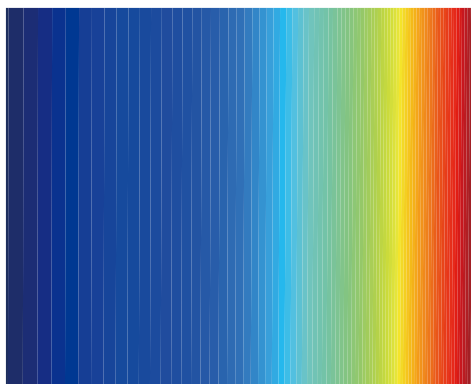


Fig. 11. Comparison of simulated and predicted gas volume fraction: (a) simulated value; (b) predicted value; (c) prediction results at the double measurement points; (d) absolute error.

pressure prediction error at any given time point is less than 10%, indicating that the physical model of gas–liquid two-phase flow in the wellbore established in this study can accurately characterize the flow behavior of each phase following a gas kick. However, it is also observed that at a few specific time points, the pressure prediction error approaches 10%, which primarily arises from numerical fluctuations caused by measurement noise during the experiment.

2

The input data used to generate the simulated pressure values at the dual measurement points, as well as the gas volume fraction and apparent gas phase velocity between the two points, are summarized in Table 2. The well has a total depth of 5000 m, and the distance between the far-bit and near-bit measurement subs is 30 m.

Fig. 7 illustrates the time-dependent responses of annulus pressure at the dual measurement points and the bottomhole gas kick rate during the gas kick process in the simulated well, after the gas front passed the far-bit measurement point. It can be observed that the annulus pressure at both measurement points gradually decreases over time, while the bottomhole gas kick rate increases progressively. This behavior is primarily attributed to the reduction in the overall fluid density in the annulus caused by the influx of formation gas, which leads to a decrease in annulus pressure. The declining annulus pressure results in an increased

pressure differential at the bottomhole, thereby accelerating the gas kick rate. As the gas kick rate increases, the fluid density in the annulus continues to decrease, further accelerating the rate of pressure decline. The temporal variations of gas volume fraction and apparent gas phase velocity exhibit similar trends to that of the gas kick rate. Therefore, the dynamic changes in annulus pressure at the dual measurement points are closely related to the gas volume fraction, apparent gas phase velocity, and gas kick rate. These parameters can thus be inferred from the annulus pressure data collected at the dual measurement points.

The maximum measurement noise of the pressure sensors was assumed to follow a uniform distribution $(0.20, \pm 0.20)$ MPa. The temporal domain was defined as $[0 \text{ s}, 2400 \text{ s}]$, and the axial spatial domain as $[4970 \text{ m}, 5000 \text{ m}]$, with a time step of 60 s and a spatial step of 5 m. As a result, a total of 195 spatiotemporal sample points were selected for fitting the mass conservation and momentum conservation equations. In addition, 82 boundary condition samples were used to fit the annulus pressure at the dual measurement points. The distribution of the training samples is shown in Fig. 8.

3 y

During the training of the PINN, the Tanh function, commonly used in PINN studies, was employed as the activation function. The batch size was set to 16, with $\eta = 0.001$, $\alpha = 0.12$, $\beta = 12,708$, and $\gamma = 300$. The initial weights for Networks A to D were initialized

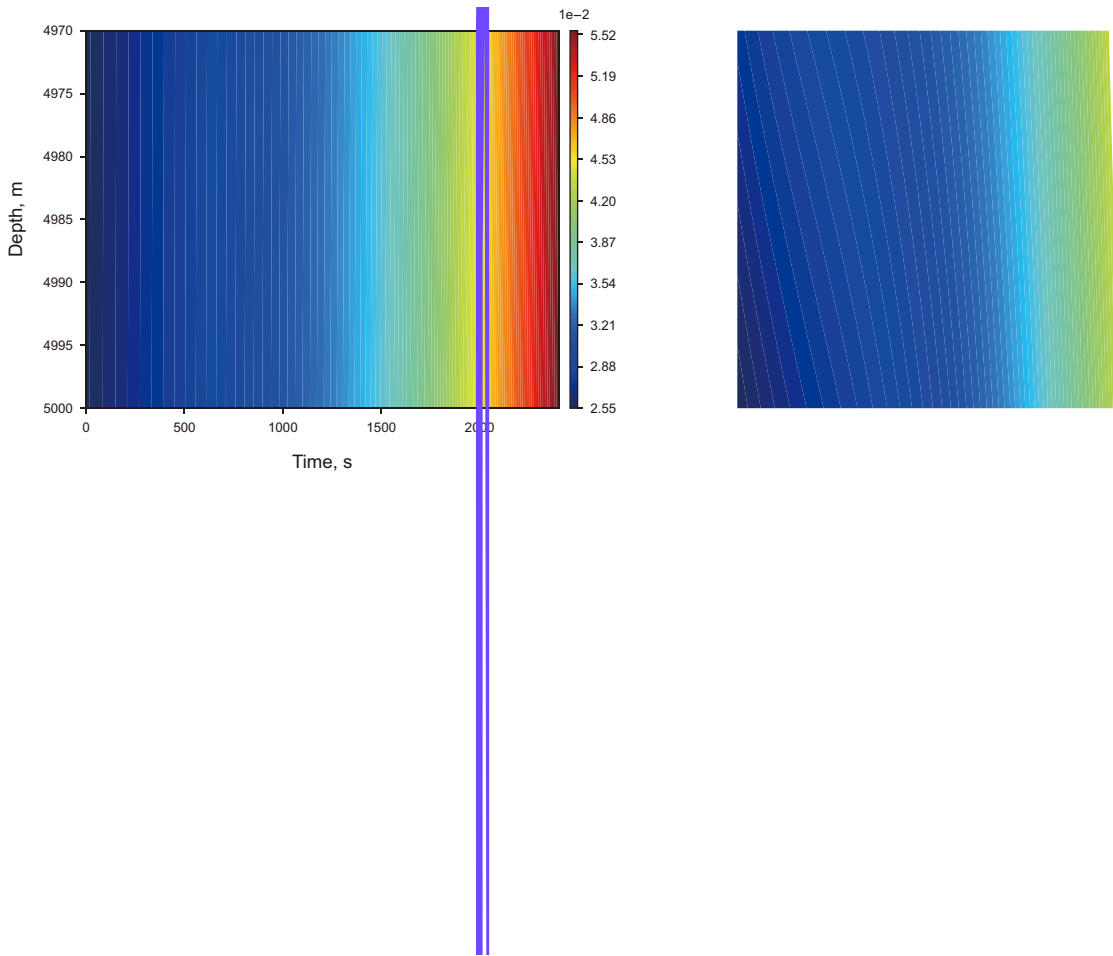


Fig. 12. Comparison of simulated and predicted apparent gas phase velocity: (a) simulated value; (b) predicted value; (c) prediction results at the double measurement points; (d) absolute error.

significantly affect the performance of the PINN. The measurement errors of the pressure sensors at the dual measurement points were assumed to follow a uniform distribution ($0.05, \pm 0.05$) MPa. Using the MRE of the bottomhole gas kick rate prediction as the evaluation metric, a controlled variable method was applied to optimize the hyperparameters. The optimization results are shown in Fig. 9. Considering both the accuracy of the quantitative interpretation of the gas kick and computational cost, the final hyperparameter settings were determined as follows: an initial learning rate of 0.001, three hidden layers for Networks A to D, eight nodes per hidden layer, and 200 and 300 iterations for the Adam and L-BFGS algorithms, respectively.

Fig. 13. Comparison of simulated and predicted apparent gas phase velocity

using the Kaiming method, and all biases were set to zero. The weights of all loss terms were initialized to 1. Each of Networks A to D had two input nodes and one output node. The initial learning rate, the number of hidden layers, the number of nodes per hidden layer, and the number of iterations for the Adam and L-BFGS optimizers were identified as hyperparameters that could

The measurement errors of the pressure sensors at the dual measurement points were assumed to follow a uniform distribution ($0.05, \pm 0.05$) MPa. The neural network structure optimized in Section 4.3 was applied to predict key parameters during the gas kick process in the simulated well, including gas volume fraction, apparent gas phase velocity, and gas kick rate. Fig. 10 illustrates the variation of each loss term (Fig. 10(a)) and the total loss (Fig. 10(b)) during the training of the PINN. In the early training stage, the Adam optimization algorithm adaptively

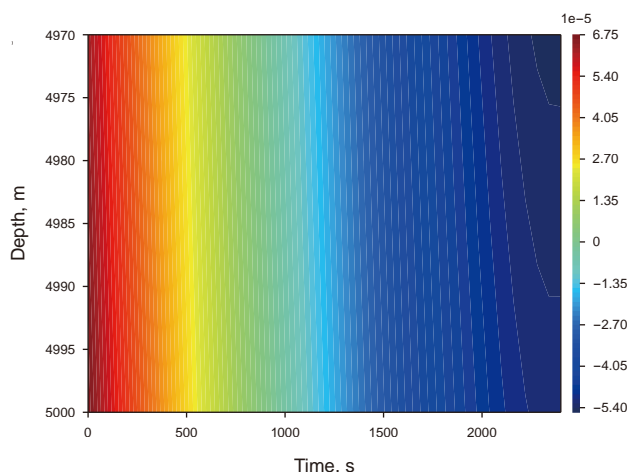


Fig. 14. Results of PINN interpretability analysis: (a) the residuals of the mass conservation equation; (b) the residuals of the momentum conservation equation; (c) prediction results for the far-bit annulus pressure; (d) prediction results for the near-bit annulus pressure.

adjusted the learning rate, enabling rapid convergence across a large parameter space. In the later stage, the L-BFGS optimization algorithm utilized second-order information to further accelerate convergence and approach the optimal solution. After 500 iterations, the total loss converged to 0.21.

Figs. 11 and 12 present comparisons between the simulated values and the predicted values for gas volume fraction and apparent gas phase velocity within the solution domain, respectively. Overall, the predicted values show a high degree of agreement with the simulated values. The MRE, RMSE, and MAE for the gas volume fraction predictions are 8.49%, 0.199%, and 0.197%, respectively. For the apparent gas phase velocity predictions, the corresponding values are 9.07%, 0.0035 m/s, and 0.0034 m/s. All MRE values are below 10%, indicating that the method can quantitatively interpret the fluid flow behavior between the dual measurement points during the gas kick based on annulus pressure data. Additionally, as shown in Figs. 11(d) and 12(d), the prediction errors for both gas volume fraction and apparent gas phase velocity at a given depth decrease over time. This trend is primarily due to the gradual increase in gas volume fraction over time. Specifically, during the early stage when the gas volume fraction is low, the gas contribution to annulus pressure at the dual measurement points is minimal, resulting in relatively stable pressure changes and larger prediction errors. As the gas volume fraction increases, its influence on the annulus pressure becomes

more pronounced. This allows the PINN to better capture the relationship between gas volume fraction, apparent gas phase velocity, and annulus pressure, leading to a reduction in prediction error over time.

Fig. 13 shows the comparison between the simulated values and the predicted values for the bottomhole gas kick rate during the gas kick process. It can be observed that the relative error of the predicted gas kick rate at each time point remains below 10%. The MRE, RMSE, and MAE are 3.76%, 0.0113 m³/s, and 0.0106 m³/s, respectively, indicating that the method accurately predicts the bottomhole gas kick rate. According to Eq. (10), the bottomhole gas kick rate is a nonlinear function of parameters such as bottomhole pressure and formation pressure. Based on the predicted gas kick rate and the measured near-bit pressure, the formation pressure can be predicted. This approach addresses the issue of prolonged shut-in pressure buildup times. The detailed method is provided in Appendix E.

Traditional purely data-driven neural networks typically function as black boxes with limited interpretability. In contrast, the neural network model trained using the PINN approach operates similarly to conventional PDE solvers, such as finite difference methods. At each spatiotemporal point within the solution domain, the model satisfies the mass and momentum conservation equations (Eqs. (31–33)) and adheres to boundary constraints at the near-bit and far-bit positions (Eqs. (34) and (35)), as

illustrated in Fig. 14. As shown in Fig. 14(a), the wave function $\psi(x)$ is a constant f_0 for $x < 0$ and zero for $x > 0$. The conservation res

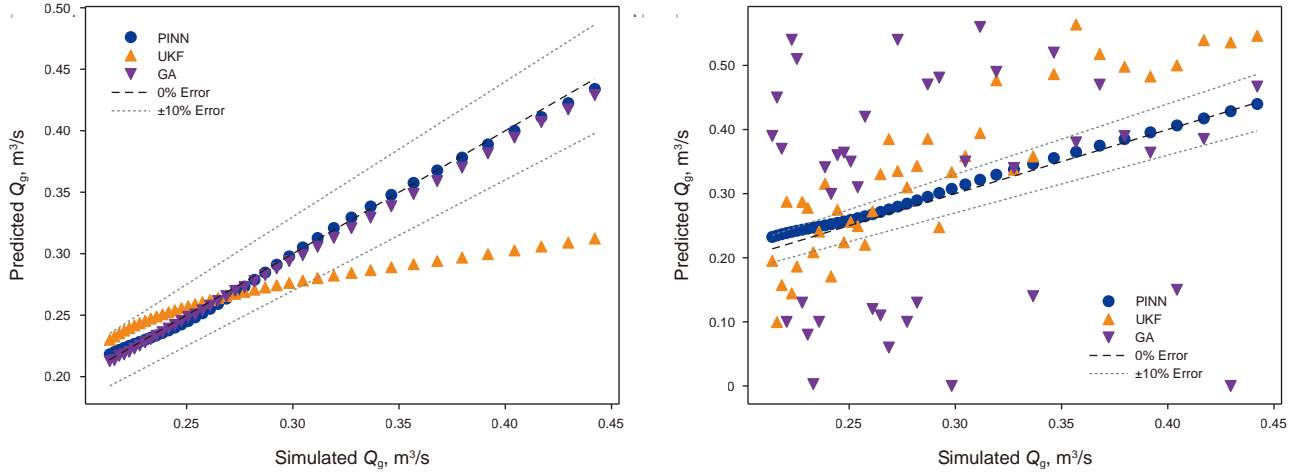


Fig. 16. Gas kick rate prediction results under two error conditions using different methods: (a) 0 MPa; (b) (0.05, ±0.05) MPa.

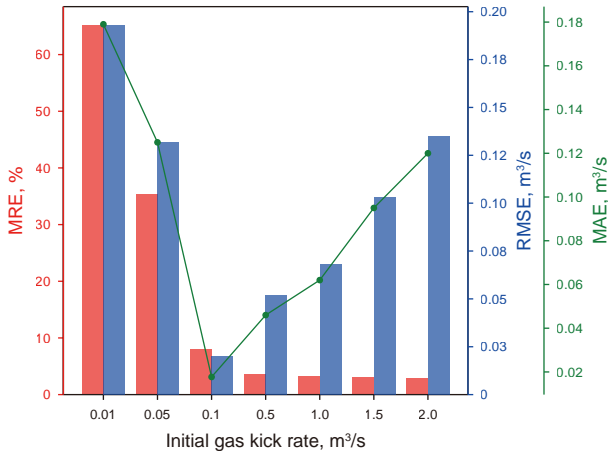


Fig. 17. Effect of gas kick rate on PINN performance.

the dual measurement points is relatively low during this period. In addition, larger momentum conservation residuals are observed near the upper and lower boundaries. This is attributed to two factors. First, fewer spatiotemporal points are distributed near the boundaries, resulting in insufficient training in these regions. Second, the network must satisfy both the governing equations and the boundary conditions near the boundaries, leading to a degree of competition that increases the residuals. Further analysis of boundary pressure prediction errors shows a high level of agreement between the predicted and simulated pressure values. For the near-bit annulus pressure (Fig. 14(d)), the MRE, RMSE, and MAE are 0.171%, 0.108 MPa, and 0.102 MPa, respectively. For the far-bit annulus pressure (Fig. 14(c)), the corresponding values are 0.167%, 0.107 MPa, and 0.099 MPa. In summary, the governing equation residuals within the solution domain and the boundary condition prediction errors meet the requirements for practical engineering applications. The trained PINN can be regarded as an approximate solver for the physical model of gas–liquid two-phase flow in the wellbore, ensuring that the relationship between inputs and outputs remains consistent with the underlying physical constraints.

2

The UKF (Xiong et al., 2006; Nikoofard et al., 2015) and the GA (Reeves and Rowe, 2002; Wang et al., 2023a) have been widely

applied for predicting wellbore fluid flow behavior. The underlying principles of these methods are not elaborated here. When applying the UKF and GA for the quantitative interpretation of gas kick, only the bottomhole gas kick rate at each time step is treated as the variable to be determined. The gas volume fraction and apparent gas phase velocity can then be directly calculated using the predicted gas kick rate and the real-time annulus pressure measurements from the dual measurement points, in combination with the physical model of gas–liquid two-phase flow in the wellbore and the finite difference method. In this study, for the UKF, the state variable is the gas kick rate, and the observation variable is the real-time annulus pressure measured at the dual measurement points. The state variable () and the observation variable () are defined as follows:

$$\hat{Q}_{g...t} \quad (54)$$

$$\hat{p}_{1...t}, \hat{p}_{2...t} \quad (55)$$

For the GA, the variable to be optimized is the gas kick rate. The objective of the optimization is to minimize the difference between the calculated and measured annulus pressures at the dual measurement points for the current gas kick rate. Accordingly, the objective function for estimating the gas kick rate using the GA is defined as:

$$\begin{aligned} & (Q_{g...t})^{\wedge} [(Q_{g...t}; 1) \quad 1...t]^2 \pm [(Q_{g...t}; 2) \quad 2...t]^2 \\ & \pm \max(0, Q_{g...t}) \end{aligned} \quad (56)$$

where, $(Q_{g...t}; 1)$ and $(Q_{g...t}; 2)$ are the calculated annulus pressures at the far-bit and near-bit positions at time t , respectively, MPa; $1...t$ is the physical model of gas–liquid two-phase flow in the wellbore.

Considering that drilling operations are conducted under complex geological conditions, factors such as severe bit vibration and drill string rotation may affect the accuracy of pressure sensor measurements. The annulus pressure measurements at the far-bit and near-bit positions serve as critical constraints for estimating gas volume fraction, gas velocity, and gas kick rate. To address this, different levels of measurement errors were assigned to the annulus pressure readings at the far-bit and near-bit positions based on the measurement accuracy of the downhole dual measurement tool. For each error condition, five repeated trials were

conducted, and the average values were used for comparative analysis. The performance and robustness of the PINN, the UKF, and the GA were evaluated under these varying error conditions. For the UKF, the standard deviation of the system noise corresponding to the state variable was set to 0.0002, and that for the observation variable was set to 0.0005. For the GA, the population size was set to 500, the maximum number of generations was 80, the crossover probability was 0.9, and the mutation probability was 0.1.

Fig. 15 presents the results obtained by the three methods under different error conditions. As the pressure sensor measurement error increases from 0 MPa to (0.20, ±0.20) MPa, the prediction accuracy for gas volume fraction, apparent gas phase velocity, and gas kick rate shows a declining trend across all three methods. This is primarily because the annulus pressure at the dual measurement points directly reflects the fluid flow behavior. As the measurement error increases, the relationship between the annulus pressure and the fluid flow behavior becomes increasingly obscure, reducing the accuracy of predictions for gas volume fraction, apparent gas phase velocity, and gas kick rate. It is also observed that when the measurement error is 0 MPa, the GA achieves the best performance, with MRE values for all three parameters below 5%. However, under all other error conditions, the PINN consistently outperforms both the UKF and the GA in prediction accuracy.

Fig. 16 illustrates the gas kick rate prediction results for the three methods under measurement error conditions of 0 MPa and (0.05, ±0.05) MPa. When noise is added to the pressure data, the prediction results from the UKF and the GA become noticeably divergent. In contrast, the PINN accurately captures the temporal variation of the gas kick rate. This is mainly because the UKF and GA tend to rely heavily on pressure measurements, making their prediction

model of gas-liquid two-phase flow in the wellbore. It also addresses the challenges posed by the scarcity of gas kick data samples, which typically result in low robustness and weak interpretability in purely data-driven neural network models. Within the solution domain, the residuals of the mass conservation equation are on the order of 10^{-5} , and those of the momentum conservation equation are on the order of 10^{-3} , allowing the trained model to function as an approximate solver for the physical model of gas-liquid two-phase flow in the wellbore.

- (2) Compared to finite difference simulation results, the mean relative errors for gas volume fraction, apparent gas phase velocity, and gas kick rate between the dual measurement points are all maintained below 10%, meeting practical engineering requirements. In addition, the proposed method demonstrates higher prediction accuracy and stability than the UKF and GA, benefiting from its global optimization strategy. Once a gas kick occurs, the method, combined with the downhole dual measurement tools, can provide essential parameter guidance for blowout risk assessment, the selection of well control methods, and the design of well control parameters.
- (3) At present, the proposed method is applicable only to drilling operations using water-based mud. In the future, efforts will be made to extend the method to oil-based mud systems, where gas dissolution in the oil-based mud will be a primary factor to consider. In addition, gas kick simulation experiments based on downhole dual-measurement tools will be conducted, and high-temperature and high-pressure well data will be used to further verify the feasibility of the proposed method.

CR

dimensions corresponding to the actual gas and liquid velocities, annulus pressure, and gas volume fraction. In this configuration, all four state parameters share a common set of model weights and biases. The second scheme, illustrated in Fig. A-2(b), assigns a separate neural network to each state parameter, ensuring that the neurons responsible for predicting the four outputs operate independently. Table A-2 presents a comparative analysis of the quantitative interpretation accuracy for gas kick achieved by the two architectural schemes. The results indicate that the second scheme yields higher prediction accuracy for the gas kick rate, gas volume fraction, and apparent gas phase velocity compared to the first scheme. Therefore, the second architectural scheme was selected for training the PINN.

C. Comparison of temperature field distributions between dual measurement points under different models.

In field applications, the proposed method utilizes the measured annulus temperature at the dual measurement points to directly calculate the temperature at any spatiotemporal location within the solution domain using Eq. (A-4) (Model 1).

$$T_{i,t} = T_{1,t} + \frac{T_{2,t} - T_{1,t}}{r_2 - r_1} (r_i - r_1) \tag{A-4}$$

where, $T_{i,t}$ is the temperature at spatial location r_i ; $T_{1,t}$ is the measured temperature at the far-bit position, r_1 ; $T_{2,t}$ is the measured temperature at the near-bit position, r_2 .



observed that both curves exhibit a consistent overall fluctuation trend with a high degree of numerical agreement, indicating that the model can reasonably reproduce the pressure variation characteristics during the gas kick process. In addition, a slight oscillation in the measured pressure is observed between 15 and 45 min, which is mainly attributed to the pump rate instability during that period. Furthermore, the pressure prediction error distribution shown in [Fig. A-5](#) demonstrates that the prediction prediction

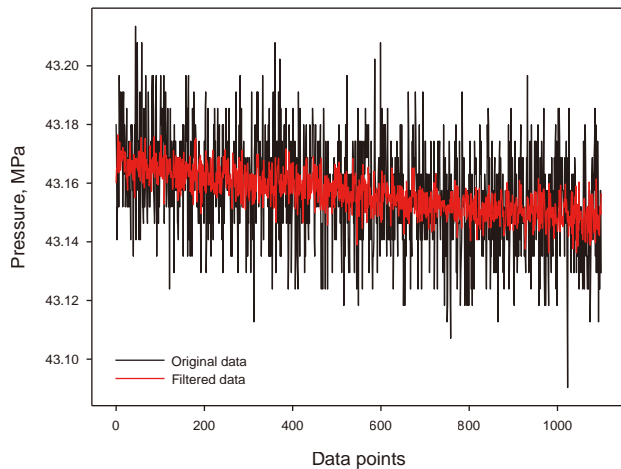


Fig. A-7. Comparison of pressure results before and after wavelet decomposition and reconstruction.

References

- Ali, T.H., Haberer, S.M., Says, I.P., et al., 2013. Automated alarms for smart flowback fingerprinting and early kick detection. In: SPE/IADC Drilling Conference and Exhibition. <https://doi.org/10.2118/163474-MS>.
- Alouhali, R., Aljubran, M., Gharbi, S., et al., 2018. Drilling through data: automated kick detection using data mining. In: SPE International Heavy Oil Conference and Exhibition. <https://doi.org/10.2118/193687-MS>.
- Amini, D., Haghighat, E., Juanes, R., 2022. Physics-informed neural network solution of thermo-hydro-mechanical processes in porous media. *J. Eng. Mech.* 148 (11), 04022070. [https://doi.org/10.1061/\(ASCE\)EM.1943-7889.0002156](https://doi.org/10.1061/(ASCE)EM.1943-7889.0002156).
- Amini, D., Haghighat, E., Juanes, R., 2023. Inverse modeling of nonisothermal multiphase poromechanics using physics-informed neural networks. *J. Comput. Phys.* 490, 112323. <https://doi.org/10.1016/j.jcp.2023.112323>.
- Atchison, B., 2022. Automated well control: a step change in safety. *Digital Chemical Engineering* 3, 100022. <https://doi.org/10.1016/j.dche.2022.100022>.
- Bhandari, J., Abbassi, R., Garaniya, V., et al., 2015. Risk analysis of deepwater drilling operations using Bayesian network. *J. Loss Prev. Process. Ind.* 38, 11–23. <https://doi.org/10.1016/j.jlp.2015.08.004>.
- Blue, D., Blakey, T., Rowe, M., 2019. Advanced mud logging: key to safe and efficient well delivery. In: Offshore Technology Conference. <https://doi.org/10.4043/29469-MS>.
- Chen, Z., Badrinarayanan, V., Lee, C.Y., et al., 2018. Gradnorm: gradient normalization for adaptive loss balancing in deep multitask networks. In: Minternational Conference on Machine Learning. <https://doi.org/10.48550/arXiv.1711.02257>.
- Colebrook, C.F., White, C.M., 1937. Experiments with fluid friction in roughened pipes. *Proceedings of the Royal Society of London. Series A-Mathematical and Physical Sciences* 161 (906), 367–381. <https://doi.org/10.1098/rspa.1937.0150>.
- Dashti, H.H., Riazi, M.R., 2014. Acoustic velocities in petroleum fluids: measurement and prediction. *J. Petrol. Sci. Eng.* 124, 94–104. <https://doi.org/10.1016/j.petrol.2014.10.013>.
- Dissanayake, M.G., Newman, P., Clark, S., et al., 2001. A solution to the simultaneous localization and map building (SLAM) problem. *IEEE Trans. Robot. Autom.* 17 (3), 229–241. <https://doi.org/10.1109/70.938381>.
- Galdino, J.F., Oliveira, G.M., Franco, A.T., et al., 2019. Gas kick detection and pressure transmission in thixotropic, compressible drilling fluids. *J. Petrol. Sci. Eng.* 180, 138–149. <https://doi.org/10.1016/j.petrol.2019.05.029>.
- Gkionis, M., Wilhelmssen, N.C.A., Aamo, O.M., 2025. Fault diagnosis for drilling using a multitask physics-informed neural network. *IFAC-PapersOnLine* 59 (6), 463–468. <https://doi.org/10.1016/j.ifacol.2025.07.189>.
- Gomez, L.E., Shoham, O., Schmidt, Z., et al., 1999. A unified mechanistic model for steady-state two-phase flow in wellbores and pipelines. In: SPE Annual Technical Conference and Exhibition. <https://doi.org/10.2118/56520-MS>.
- Gravdal, J.E., Lorentzen, R.J., Time, R.W., 2010. Wired drill pipe telemetry enables real-time evaluation of kick during managed pressure drilling. In: SPE Asia Pacific Oil and Gas Conference and Exhibition. <https://doi.org/10.2118/132989-MS>.
- Gu, C., Li, Q., Ma, R., et al., 2021. Propagation characteristics of doppler ultrasonic wave in gas-liquid two-phase flow in an offshore deepwater riser. *Nat. Gas. Ind. B* 8 (6), 615–621. <https://doi.org/10.1016/j.ngib.2021.11.009>.
- Hauge, E., Aamo, O.M., Godhavn, J.M., 2012. Model-based estimation and control of in/out-flux during drilling. In: 2012 American Control Conference (ACC). <https://doi.org/10.1109/ACC.2012.6315027>.
- Indimath, S., Fiorentini, S., Bøklepp, B.R., et al., 2023. Effect of bubble size on ultrasound backscatter from bubble clouds in the context of gas kick detection in boreholes. *Sci. Rep.* 13 (1), 11825. <https://doi.org/10.1038/s41598-023-38937-6>.
- Jan, A., Mahfoudh, F., Draškovic, G., et al., 2022. Multitasking physics-informed neural network for drillstring washout detection. In: 83rd EAGE Annual Conference & Exhibition. <https://doi.org/10.3997/2214-4609.202210607>.
- Jeong, C., Yu, Y., Mansour, D., et al., 2020. A physics model embedded hybrid deep neural network for drillstring washout detection. In: SPE/IADC Drilling Conference and Exhibition. <https://doi.org/10.2118/199629-MS>.
- Jiang, H., Liu, G., Li, J., et al., 2019. Numerical simulation of a new early gas kick detection method using UKF estimation and GLRT. *J. Petrol. Sci. Eng.* 173, 415–425. <https://doi.org/10.1016/j.petrol.2018.09.065>.
- Johnson, A., Leuchtenberg, C., Petrie, S., et al., 2014. Advancing deepwater kick detection. In: SPE/IADC Drilling Conference and Exhibition. <https://doi.org/10.2118/167990-MS>.
- Kapoor, T., Wang, H., Núñez, A., et al., 2023. Physics-informed neural networks for solving forward and inverse problems in complex beam systems. *IEEE Trans. Neural Networks Learn. Syst.* 35 (5), 5981–5995. <https://doi.org/10.1109/TNNLS.2023.3310585>.
- Karimi Vajargah, A., Miska, S.Z., Yu, M., et al., 2013. Feasibility study of applying intelligent drill pipe in early detection of gas influx during conventional drilling. In: SPE/IADC Drilling Conference and Exhibition. <https://doi.org/10.2118/163445-MS>.
- Lafond, A., Leblay, F., Roguin, G., et al., 2019. Automated influx and loss detection system based on advanced mud flow modeling. In: SPE Annual Technical Conference and Exhibition. <https://doi.org/10.2118/195835-MS>.
- Li, S., 2008. *Natural Gas Engineering*. Petroleum Industry Press, Beijing.
- Li, X., Zhang, J., Tang, X., et al., 2022. Propagation characteristics and application effects of measurement-while-drilling pressure wave for early gas-kick detection. *J. Loss Prev. Process. Ind.* 76, 104741. <https://doi.org/10.1016/j.jlp.2022.104741>.
- Li, Z., Yin, Q., Guo, Y., et al., 2022. A special thread design based on TC4 titanium alloy and its successful application in offshore extended-reach drilling. In: International Conference on Offshore Mechanics and Arctic Engineering (ICOMAE). <https://doi.org/10.1115/OMAE2022-80261>.
- Liu, Z., Ma, Q., Cai, B., et al., 2021. Risk assessment on deepwater drilling well control based on dynamic Bayesian network. *Process Saf. Environ.*

- Sule, I.O., Khan, F., Butt, S., 2019. Experimental investigation of gas kick effects on dynamic drilling parameters. *J. Pet. Explor. Prod. Technol.* 9, 605–616. <https://doi.org/10.1007/s13202-018-0510-z>.
- Sun, B., Sun, X., Wang, Z., et al., 2017. Effects of phase transition on gas kick migration in deepwater horizontal drilling. *J. Nat. Gas Sci. Eng.* 46, 710–729. <https://doi.org/10.1016/j.jngse.2017.09.001>.
- Sutton, R.P., 2009. An improved model for water-hydrocarbon surface tension at reservoir conditions. In: SPE Annual Technical Conference and Exhibition. <https://doi.org/10.2118/124968-MS>.
- Toskey, E.D., 2015. Kick detection at the subsea mudline. In: Offshore Technology Conference. <https://doi.org/10.4043/25847-MS>.
- Udegbunam, J.E., Fjelde, K.K., Evje, S., et al., 2014. A simple transient flow model for mpd and ubd applications. In: SPE/IADC Managed Pressure Drilling and Underbalanced Operations Conference and Exhibition. <https://doi.org/10.2118/168960-MS>.
- Walczak, B., Massart, D.L., 1997. Noise suppression and signal compression using the wavelet packet transform. *Chemometr. Intell. Lab. Syst.* 36 (2), 81–94. [https://doi.org/10.1016/S0169-7439\(96\)00077-9](https://doi.org/10.1016/S0169-7439(96)00077-9).
- Wang, J., Sun, B., Li, H., et al., 2017. Early gas kick detection based on the LWD resistivity in deepwater drilling. *Journal of China University of Petroleum (Edition of Natural Science)* 41 (6), 94–100. <https://doi.org/10.3969/j.issn.1673-5005.2017.06.011> (in Chinese).
- Wang, X., Guan, Z., Xu, Y., et al., 2018. Signal analysis of acoustic gas influx detection method at the bottom of marine riser in deepwater drilling. *J. Process Control* 66, 23–38. <https://doi.org/10.1016/j.jprocont.2017.12.008>.
- Wang, N., Zhang, D., Chang, H., et al., 2020. Deep learning of subsurface flow via theory-guided neural network. *J. Hydrol.* 584, 124700. <https://doi.org/10.1016/j.jhydrol.2020.124700>.
- Wang, C., Liu, G., Li, J., et al., 2020a. Non-uniform temperature distribution's impact on downhole weight on bit measurement (DWOB) and the novel compensatory method. *J. Petrol. Sci. Eng.* 184, 106528. <https://doi.org/10.1016/j.petrol.2019.106528>.
- Wang, C., Liu, G., Yang, Z., et al., 2020b. Downhole gas-kick transient simulation and detection with downhole dual-measurement points in water-based drilling fluid. *J. Nat. Gas Sci. Eng.* 84, 103678. <https://doi.org/10.1016/j.jngse.2020.103678>.
- Wang, Z., Zhou, W., Shu, T., et al., 2022. Modelling of low-frequency acoustic wave propagation in dilute gas-bubbly liquids. *Int. J. Mech. Sci.* 216, 106979. <https://doi.org/10.1016/j.ijmecsci.2021.106979>.
- Wang, B., Li, J., Zhang, G., et al., 2023. A novel early gas kick monitoring method using the difference between downhole dual measurement points pressure and a genetic algorithm-based model. *Geoenergy Sci. Eng.* 231, 212371. <https://doi.org/10.1016/j.geoen.2023.212371>.
- Wang, Z., Chen, G., Zhang, R., et al., 2023. Early monitoring of gas kick in deepwater drilling based on ensemble learning method: a case study at South China Sea. *Process Saf. Environ. Prot.* 169, 504–514. <https://doi.org/10.1016/j.psep.2022.11.024>.
- Wu, X., Hu, X., Han, L., et al., 2022. Research progress and the prospect of well control technology. *Nat. Gas. Ind.* 42 (2), 133–142. <https://doi.org/10.3787/j.issn.1000-0976.2022.02.014>.
- Xia, A.D., Sun, B.J., Yu, X.D., et al., 2019. Gas kick type determination and formation information calculation based on gas kick response parameters. In: *International Petroleum and Petrochemical Technology Conference & Exhibition, Beijing, China*.
- Xiong, K., Zhang, H.Y., Chan, C.W., 2006. Performance evaluation of UKF-Based nonlinear filtering. *Automatica* 42 (2), 261–270. <https://doi.org/10.1016/j.automatica.2005.11.024>.
- Xu, B., Zhang, X., Wang, Y., et al., 2023. Self-adaptive physical information neural network model for prediction of two-phase flow annulus pressure. *Acta Pet. Sin.* 44 (3), 545–555. <https://doi.org/10.7623/syxb202303012> (in Chinese).
- Yan, B., Harp, D.R., Chen, B., et al., 2022. A gradient-based deep neural network model for simulating multiphase flow in porous media. *J. Comput. Phys.* 463, 111277. <https://doi.org/10.1016/j.jcp.2022.111277>.
- Yang, X., Zhang, S., Zhu, W., 2017. A new model for the accurate calculation of natural gas viscosity. *Nat. Gas. Ind.*